JOURNAL OF AIRCRAFT
Vol. 43, No. 4, July–August 2006

Numerical Simulations for Transport Aircraft High-Lift Configurations Using Cartesian Grid Methods

Weimin Sang* and Fengwei Li†
Northwestern Polytechnical University, 710072 Xi'an, Shaanxi, People's Republic of China

Computations of complex flow fields around three-dimensional high-lift configurations using an adaptive Cartesian grid method and a cell-center finite-volume method are carried out and compared to wind-tunnel experiments. Because of complexities in both configuration and flowfield, there are great difficulties in numerical simulation of flowfields around transport aircraft high-lift configurations with leading slats and trailing flaps. In this paper, a modified Cartesian grid method is introduced to simulate the complex flow using the adaptive grid technique. The main emphasis is given to a multizone technique and a face-to-face algorithm and its applications. The multizone technique is employed to simplify the great difficulties in grid generation. The face-to-face algorithm is constructed to precisely establish the information exchange of flowfields on interfaces between zones. We solve Euler equations with a conventional algorithm, which includes a cell-center finite-volume method and an explicit four-stage Runge–Kutta time-stepping scheme in combination with a dual-time stepping approach. For three three-dimensional high-lift configurations, the numerical results are presented and analyzed. The computational results are in good agreement with the available experimental data show that the present method is feasible and effective for solving the flow around complex three-dimensional high-lift systems.

Introduction

DURING landing and takeoff, a modern transport aircraft usually employs slats and flaps to form a high-lift configuration in order to provide sufficient lift. In contrast to cruise configurations, where the wing consists of a single geometry, these high-lift devices are separated from the main wing element by very small gaps. Computational fluid dynamics (CFD) is playing an increasingly important role in the aerodynamic design of aircraft. To reduce wind-tunnel test costs and design cycle time, significant efforts are now under way in the development of CFD techniques for the prediction of high-lift flows.

Aside from continuous development and increasing experience in applying grid methods and flow solvers to two-dimensional high-lift problems (for example, see Refs. 1–4), comparatively few examples of three-dimensional high-lift applications for realistic aircraft configurations have been reported. The reason is basically the high degree of geometrical complexity of deployed high-lift systems in conjunction with a variety of relevant flow features, such as strong pressure gradients and geometry-induced separation. Although the range of working speeds is limited to low Mach numbers, due to the flow acceleration, shock waves and shock/boundary interactions may still occur inside the narrow gaps between slat and main wing. The geometry of the three-dimensional high-lift configuration is characterized by both multielements and the existence of geometric discontinuities at places such as flap ends, which can cause severe difficulties for the grid generation approach. Because of the inherent complexities of three-dimensional high-lift flows (both geometric and physical flows), the accurate analysis of such flows requires a high-quality grid. The consideration of such problems gives rise to significant challenges not only in the flow solution process, but also in the grid generation procedure. With the improvements that have occurred over the years, CFD methods play an increasingly important role in supporting the three-dimensional high-lift design process.

Thus, to compute three-dimensional high-lift flows, complex grid generation strategies must be constructed and utilized. Some three-dimensional of numerical simulations of flow over multielement configurations have already been reported. These studies range from the early work of Rogers[5] to recent studies by Peter[6] and Rudnik et al.[7] In 1995, Mathias[8] used structured grids code to compute the flow around a two-element upswept wing with a part-span flap. Some investigations have addressed more realistic high-lift geometries. For example, Cao et al.[9] applied and evaluated the overset grid method for a Boeing 747PD high-lift configuration. Many of the improvements concern flow computations using multiblock structured grids and overlapping block structured grids. But there are some contributions using unstructured grids. Because of geometric complexities, as well as the associated intense resource requirements for three-dimensional high-lift CFD methods, reports on the unstructured grid method in three-dimensional high-lift applications are limited. Unstructured grid techniques offer the potential for greatly reducing the grid generation time associated with complex three-dimensional high-lift configurations. Furthermore, compared to structured grids, unstructured mesh approaches enable the use of adaptive meshing techniques that hold great promise for increasing the accuracy of solution at minimal additional computational cost. However, unstructured mesh solvers require significantly higher computational resources than their structured grid counterparts, thus limiting their applicability for large three-dimensional calculations.

In this paper, emphasis is placed on the grid generation method. Our goals here are to modify an adaptive Cartesian grid method through the use of a multizone technique and a face-to-face algorithm to highlight the prominent changes in the grid generation of the numerical simulation of flowfields over three-dimensional high-lift configurations. In contrast to previous studies that concentrate on a single solution approach, such as the multiblock grids method in Ref. 6, the chimera technique in Ref. 8, or the hybrid unstructured approach of Ref. 7, the present work offers the possibility of extending the applications and capabilities of the Cartesian grid method.

To provide designers with a three-dimensional high-lift analysis tool for preliminary aerodynamic designs, we recently developed a CFD code based on the adaptive Cartesian grid method. The code consists of a grid generator and a flow solver. The core methodology is a multizone technique and a face-to-face algorithm, which solves

Received 29 May 2005; presented as Paper 2005-4965 at the AIAA 23rd Applied Aerodynamics Conference, Toronto, ON, 6–9 June 2005; revision received 12 September 2005; accepted for publication 13 September 2005.

*Associate Professor, P.O. Box 114, School of Aeronautics; xhasang@sina.com.

†Professor, P.O. Box 114, School of Aeronautics. Member AIAA.

the three-dimensional high-lift problems that accompany multielement and geometrical discontinuities very well. By the use of the adaptive Cartesian grid method, the grid construction procedure is simplified and the required number of grid points can generally be reduced. This paper introduces the ideas and methodologies employed in the CFD code. The capability and performance of the code for high-lift computation are assessed in numerical simulations of three test models with deployed high-lift systems. These models contain high-lift wing geometries with part-span flap elements and wing/body configurations with slats and flaps. Complete details of the computational grids and numerical solver are given. Using a dual-time stepping scheme, an explicit four-stage Runge–Kutta algorithm based on the cell-center finite volume method (CCFVM) for the Euler equations has been developed that is applicable to the Cartesian grids. Computed results and comparisons with experimental data are presented and analyzed.

Grid Generation Methods

Tree Data Structure

The tree data structure is the roadmap of the information in the course of Cartesian grid generation.

A quadtree-based data structure is ideally suited for the two-dimensional Cartesian grid scheme. This concept is illustrated in Fig. 1. The tree data structure begins with one root cell defined at depth 0. When this cell is refined, four child cells of equal size are created at one higher depth 1. In turn, these cells are refined again until a suitable grid has been created. From this basic structure, all other needed information about the relative position of any cell can be determined.

In three-dimensional Cartesian grid generation, we use an Octree data structure to store grid information about nodes, lines, faces, and cells. All elements of the grid are handled by a single unifying edge-based data structure that has been proven to be effective in the flow solver.

Adaptive Cartesian Grids

The Cartesian grid method uses a non-body-fitted grid to discretize the flow field about an object. The Cartesian grid is generated from one large root cell that covers the entire computational domain. The root Cartesian cell is subdivided recursively until a user-specified minimum grid solution is obtained. After creating this surrounding grid, the surface geometry is simply cut out from the intersecting cells, leaving a border of irregular cells surrounding the object surface. In this paper, we generate the Cartesian grids using a cell-cutting algorithm. Details of the algorithm are described in Ref. 10.

For one three-dimensional high-lift configuration, the accessorial parts are usually relatively small in size and often need finer grids to reveal the geometry and flow details. The generation of the computational grid is accomplished using an adaptive grid technique, which is one important aspect in the Cartesian grid method. The geometry-based grid adaptation offers the ability to adjust the grid resolution quite flexibly in the relevant areas of the configuration. The adaptation is based on a geometry curvature sensor, resulting in a higher grid resolution at the leading edges and trailing edges

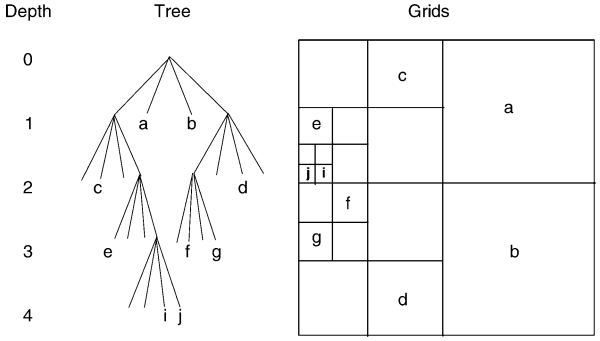

Fig. 1 Tree data structure in grid generation.

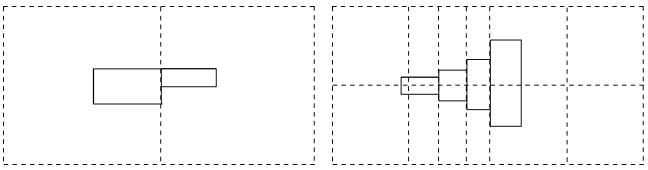

a) Single discontinuity view **b) Multidiscontinuity view**

Fig. 2 Illustration of the multizonal root cell.

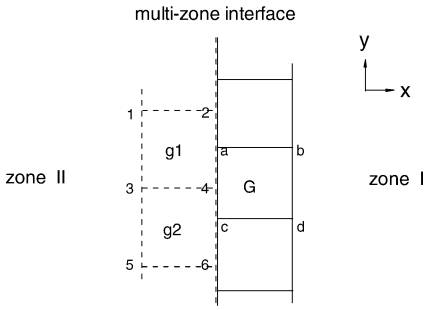

Fig. 3 Two-dimensional map for the multizone interface.

as in the structured grids. Based on a well-defined CAD description of the model, the grid generation process requires less time than the structured grid method, depending on the grid point number, adaptation steps, and hardware availability.

In our grid generation task, the main development is directed at dealing with complex and discontinuous geometry for the adaptive Cartesian grid method. Therefore, discussion focuses on a multizone technique and a face-to-face algorithm, which are described in the following sections.

Multizone Technique

The requirement for the multizone technique will increase the flexibility in arranging grid density and topology in the grid zones. In generating multizone grids, the defining of the multizone boundaries usually demands a great deal of manual labor and manipulation. In our multizone technique, this time-consuming labor can be avoided. The interface boundaries are constructed along discontinuous surfaces of the high-lift configuration. No more geometric modeling is needed. In this sense, the multizone technique can be automated with greater ease.

The multizone interface is generated in the initial root cell. One root cell becomes more root cells using the multizone technique. The process is shown as a two-dimensional map in Fig. 2. The solid lines represent the model boundaries, and the dashed lines represent the multizone boundaries. Note that the discontinuity on the geometry is overlaid with some dashed lines. In Fig. 2, 2a and 2b respectively represent the multizone grid generation of cases 1 and 3 in the *Numerical Results* section.

Once the zones have been constructed, the restart capability of the Cartesian grid generator is appropriate to incorporate moderate changes in wing shape or the high-lift setting. To smooth grids in the adaptive process, the grid clustering in one zone will often have to be extended to an adjacent zone, where no clustering is needed.

Face-to-Face Algorithm

Flux Computation

When geometric discontinuity exists, the technique of overlapping area-weighted reconstruction (OAWR) of flux parameters is used for flowfield information exchange to allow grid cells discontinuous interfacing. OAWR was developed by Kathong et al. (Ref. 11) and is used by many CFD researchers. To explain the idea of the OAWR, the procedure of flux computation on a two-dimensional multizone interface is described in the following.

In Fig. 3, grid cells in zones I and II patched on the multizone interface are drawn by solid and dashed lines and labeled by symbols G, g1, and g2, respectively. In the Cartesian grids, cells G, g1, and g2 have four vertexes and four faces as shown in Fig. 3.

As in the flow solver code, the conservative flow variables are stored at the cell center. According to the CCFVM, the flux on face $\overline{ac}$ of cell G can be written as

$$\mathrm{FLUX}_{\overline{ac}} = [(\boldsymbol{F}_G + \boldsymbol{F}_{g1})/2]S_{\overline{a4}} + [(\boldsymbol{F}_G + \boldsymbol{F}_{g2})/2]S_{\overline{4c}} \qquad (1)$$

where $\boldsymbol{F}$ is the conservative variable, $S_{\overline{a4}}$ and $S_{\overline{4c}}$ are the area of cell G's overlap with cells g1 and g2 on the multizone interface, and the sum of $S_{\overline{a4}}$ and $S_{\overline{4c}}$ is the area of the face $\overline{ac}$.

Thus, the interface flux computation depends on the overlap area between adjacent zone boundary cells. From the deduction procedure, it is easy to understand that, when incorporated into CCFVM, this technique guarantees the global flux conservation at the multizone interface.

In three-dimensional cases, the above idea is still applicable and feasible. The overlap relation between adjacent zone boundary cells may be so complex that we have to use the following face-to-face algorithm to determine the overlap area in Eq. (1).

Face-to-Face Algorithm

Because the data structure is based on the edges of the control volume, the face-to-face algorithm is independent of the type of grid cells, allowing it to handle either cut or noncut cells. According to the multizone technique in Cartesian grid generation, all zones are constructed in one large root cell. Thus, at the multizone interface, cell faces are matched strictly for adjacent zone boundary cell faces, and mismatch does not occur here.

In the three-dimensional Cartesian grids, the basic face element is a quadrangle. The face-to-face algorithm in our CFD code is based on the surface patch technique. If two cells are noncut cells, the overlap relation is very simple. Otherwise, the overlap relation is complex if there is one cut cell at the multizone interface. Thus, four patch patterns may occur for interfacing between different zones, as presented in Fig. 4. Note that every pattern in Figs. 4a–4d shows faces of two cells at the multizone interface. The number and position of the faces are different.

Let m and n be the numbers of faces of two cells in adjacent zones; then at the multizone interface,

1) If $m = 1$ and $n = 1$ and there is one noncut face, see Fig. 4a. In this figure, A represents the noncut face and C is the other cut face. B represents the area difference between A and C.

2) If $m = 1$ and $n = 1$ and there are two cut faces, see Fig. 4b. Note that point c is the intersectional point between boundary lines of two faces. It is key for overlap area computation.

3) If $m > 1$ or $n > 1$, see Fig. 4c. In this figure, $m = 1$ and $n = 4$. It resembles the pattern in Fig. 4a.

4) If $m > 1$ and $n > 1$, see Fig. 4d. The pattern can only occur when $m = 2$ and $n = 2$. In the same way, points c0 and c1 are the intersectional point between boundary lines of two faces.

From the above face-to-face patch process, an obvious overlap relation can be found, and the overlap area can be determined easily.

The patch technique reduces the tedious work of dealing with the mutual restrictions of grid topology and density between zones in grid generation. Hence, appropriate grid density and topology can be arranged principally according to the flow and geometry requirement. With the patch methods, flowfield information is exchanged, during the numerical computation, in a conserved manner between grid cells in different zones.

The multizone and face-to-face techniques are somewhat like a combination of the Chimera grid technique and the patch grid technique. On the one hand, the code takes advantage of the Chimera technique's embedding idea, which makes it able to decompose a complex configuration into clean parts and then generate grids for them separately. On the other hand, unlike the Chimera grid technique, the grid blocks are clearly separated by interface surfaces. No grid overlap occurs in the method. Therefore, no spatial interpolation in flow quantities of different grid cells, which is often the cause of lack of conservation in the numerical computation, is required.

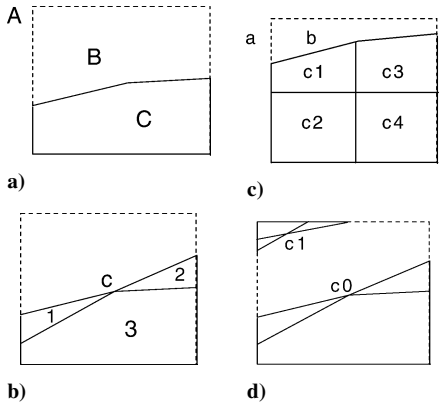

Fig. 4 Plane illustration of patch technique on the multizone interface.

Numerical Methods

Euler Flow Solver

The governing equations are solved on a refined grid, which is determined directly from the initial grid.

The flow solver code is characterized by a cell center finite volume formulation of the Euler governing equations. The unsteady, compressible Euler equations in integral form are

$$\frac{\partial}{\partial t}\int_{\Omega} W \,\mathrm{d}\Omega + \int_{S} \boldsymbol{F}\cdot\boldsymbol{n}\,\mathrm{d}s = 0 \qquad (2)$$

where Ω is the control volume, and S is the boundary.

As used for the present computations, the cell-centered finite volume methods are employed to solve the Euler equations. According to Stolcis and Johnston (see Ref. 12), the Jameson-type blended second- and fourth-order artificial viscosity is added to the essentially central differencing spatial scheme for the suppression of the spurious numerical oscillation. Time integration to steady state is accomplished using an explicit four-stage Runge–Kutta time-stepping scheme in conjunction with local time stepping and implicit residual smoothing to accelerate the convergence process.

At the farfield boundary some special boundary conditions must be imposed. At the solid surface boundary the impermeable boundary condition is applied; that is, the normal flux is zero.

The governing equation (2) is discretized using cell-centered finite volume methods. The following semidiscrete system of nonlinear equations is used for a given grid cell i:

$$\frac{\partial}{\partial t}(V_i W_i) + Q_i = 0 \qquad (3)$$

where V_i and Q_i are the volume of the given cell and the net convective flux, respectively.

Dual-Time Stepping Scheme

A dual-time stepping algorithm is used to improve the robustness, efficiency, and accuracy of the flow solver. For Eq. (3), we can solve using the explicit four-stage Runge–Kutta time-stepping scheme. At physical time step $n+1$, this equation may be written as

$$\frac{\partial}{\partial t}\left(V_i W_i^{n+1}\right) + Q_i^{n+1} = 0 \qquad (4)$$

According to Refs. 13 and 14, a Newton-like subiteration is introduced through a pseudo-time τ to write the solving problem for the pseudo-steady state as

$$\frac{\partial}{\partial \tau}(V_i W_i) + \frac{\partial}{\partial t}\left(V_i W_i^{n+1}\right) + Q_i^{n+1} = 0 \qquad (5)$$

Using backward first-order and second-order accuracy time-difference formulae to discretize the above derivative items, Eq. (5) becomes

$$\frac{W_i^{m+1} - W_i^m}{\Delta\tau} + \frac{3W_i^{n+1} - 4W_i^n + W_i^{n-1}}{2\Delta t} + R_i^{n+1} = 0$$

$$R_i^{n+1} = \frac{Q_i^{n+1}}{V_i} \qquad (6)$$

thus

$$\frac{W_i^{m+1} - W_i^m}{\Delta\tau} = -R_i^{m+1}$$

$$R_i^{m+1} = \frac{3W_i^{n+1} - 4W_i^n + W_i^{n-1}}{2\Delta t} + R_i^{n+1} \tag{7}$$

where m denotes the pseudo-time.

The initial values for the subiteration are taken as $W_i^m = W_i^n$. Starting from $m = 1$, $W_i^1 = W_i^n$ the sequence of iterations W_i^m, $m = 1, 2, 3, \ldots$, converges to W_i^{n+1} when the right-hand side residual is equal to zero. Thus, through subiteration in the pseudo-time, the following equation is valid:

$$\frac{3W_i^{n+1} - 4W_i^n + W_i^{n-1}}{2} + \Delta t R_i^{n+1} = 0 \tag{8}$$

At convergence of the pseudo-time iterations $\Delta W^m \to 0$, the accuracy of the solution at each physical time step is the accuracy of the discretized unsteady governing equations. That is to say, in the case of convergence, $W_i^{m+1} \to W_i^{n+1}$ and $R_i^{m+1} \to R_i^{n+1}$.

Substituting $R_i^{n+1} = Q_i^{n+1}/V_i$ into the above equation yields a fully second-order implicit scheme in time for the governing equation:

$$V_i \frac{3W_i^{n+1} - 4W_i^n + W_i^{n-1}}{2\Delta t} + Q_i^{n+1} = 0 \tag{9}$$

The computing practices show that the convergence rate with the pseudo-time process is very fast, and only a few subiteration steps are needed. For some steady-state flow problems, this dual-time stepping scheme allows a large pseudo-time step, enabling fast convergence.

Numerical Results

The presented results will focus on three-dimensional high-lift configurations with geometric discontinuity. The numerical results are compared to the experimental results obtained from a wind tunnel to assess the CFD capabilities, numerical solver, and grid generation method.

The main emphasis of the present contribution is to demonstrate and to discuss the CFD improvements obtained in the adaptive Cartesian grid method. Flowfields about the three models of the three-dimensional high-lift configuration have been studied and are numericaly simulated using the above grid generation method and flow solver.

Case 1: Two Partial-Span Flap Wing

The system is composed of a main element and a part-span flap as shown in Fig. 5. The flap deflection was set at 29 deg. In the grid generation, an initial Cartesian grid is first generated after the multizone technique is finished. According to the shape of the configuration, there are two zones in the computational domain divided by the midspan section. Because small gaps in position are significant in the flow computation, three adaptive refinements were done after initial grid generation to describe exactly the geometrical gap and overhang setting. Some grid clustering was used in the nonflapped section of the main wing to support grid refinement at the flap edge.

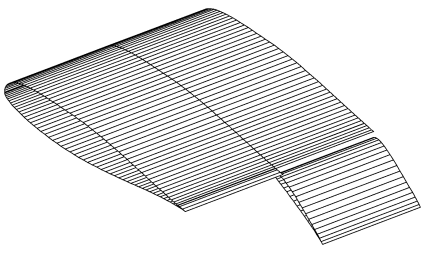

Fig. 5 Model geometry.

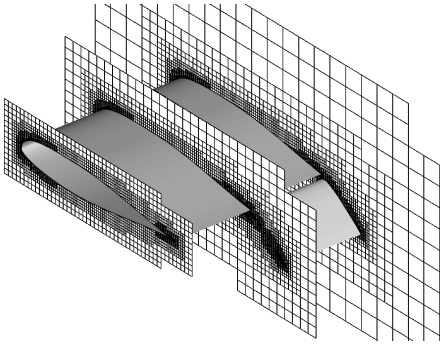

Fig. 6 Computational grids.

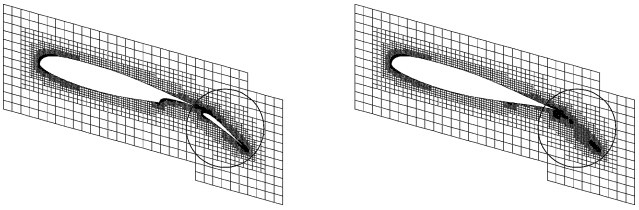

Fig. 7 Comparison of grid sections on the multizone interface.

Then, as shown in Fig. 6, a computational grid of high quality is generated, which has 2.1×10^5 grid cells. At the multizone interface, two zone grid faces are comprised in Fig. 7. Most differences focus on the flapped and nonflapped position labeled by a circle in figure.

The experimental data in Ref. 15 are used and conducted at a freestream Mach number of 0.22 and an angle of attack of 10 deg. Convergence to a steady-state solution was assumed when there were no changes in the lift and drag coefficients to five significant digits with subsequent iterations. Figure 8 compares the computational and experimental surface pressure distributions at four spanwise locations. Two of the spanwise stations are in the flapped region of the wing and the other two are in the nonflapped segment of the wing. As is shown, the computations are in good agreement with the experimental data. Figure 9a shows the Mach contours at two symmetry sections, and the extent of the flow disturbance due to the flap on both flapped and nonflapped segments of the wing. Figure 9b presents the computed Mach number contour on section at the 28% spanwise location. The contour plot shows significant acceleration of the flow through the gap, causing the Mach numbers in the vicinity of the main element and flap leading edges to approach a value nearly twice the freestream Mach number of 0.2.

Case 2: Wing/Body High-Lift Configuration

The subject geometry consists of a fuselage, wing, and trailing edge flap in a high-lift position and involves complexities such as sharp corners and small gaps between multiple components. The flap starts at 20% half span and ends at 70% half span with a deflection angle of 35 deg. Figure 10 shows the whole geometry as simulated.

The multizone technique is used to construct four spanwise zones on the whole domain. To ease the computational task and reduce the number of grid points required, the grid adaptive technique based on the geometry is finished twice. Figures 11a and 11b present the generated grids, which consist of 3.4×10^5 grid cells.

The model has been experimentally studied in the low-speed wind tunnel at Nanjing Universality of Aeronautics and Astronautics (NUAA). The size of the test section in the wind tunnel is 3×2.5 m. In the model test, measurements were taken at freestream Mach number 0.2.

Figure 12 shows a corresponding pressure distribution at four spanwise stations for angles of attack 4.47 and 8.65 deg. In general, the deviations are small on the main wing upper surface; most differences occur on the whole upper surface of the flap. The reason for this difference is attributed to the present Euler flow solver

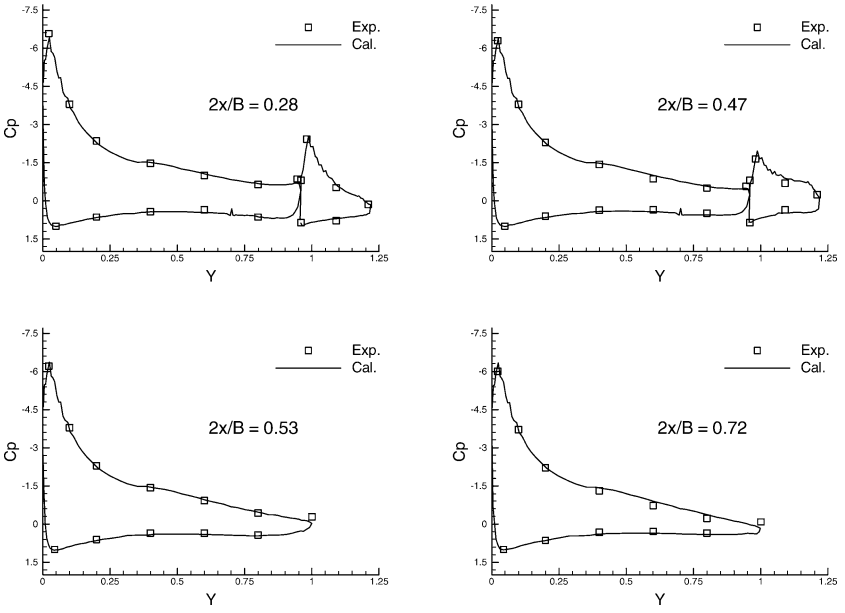

Fig. 8 Comparison between computed and experimental surface pressure coefficients ($M_\infty = 0.22$, $\alpha = 10.0$ deg).

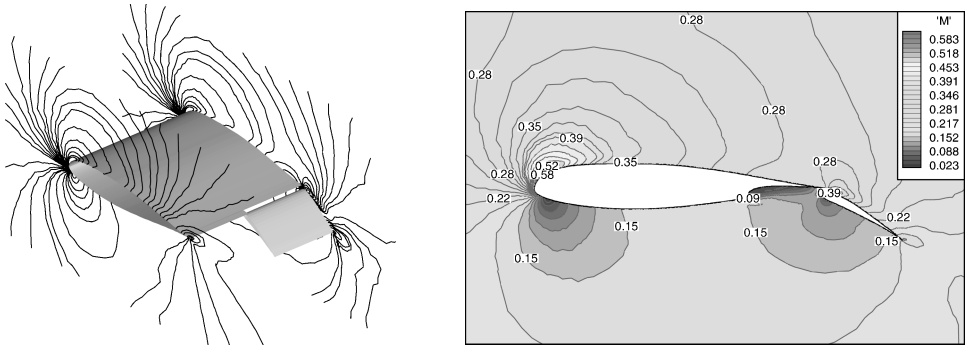

a) On the symmetry sections **b) On section at 28% spanwise location**

Fig. 9 Computed mach contours.

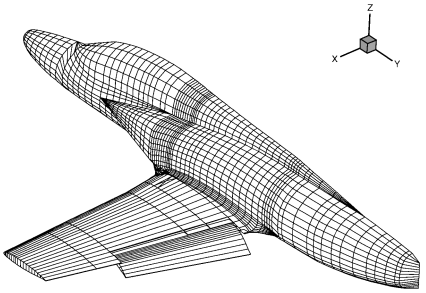

Fig. 10 Model geometry.

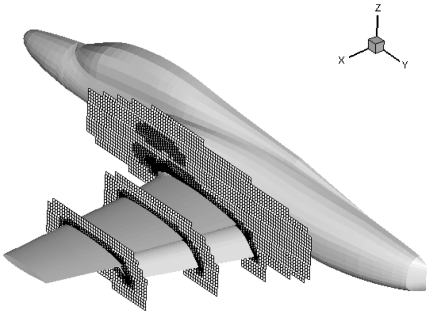

a) Cross-sectional view

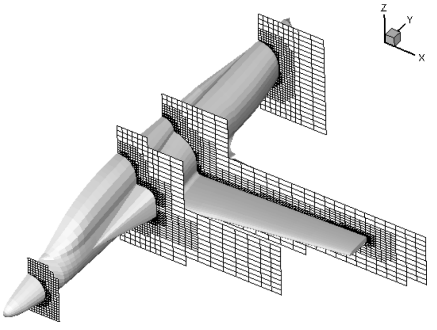

b) Axial sectional view

Fig. 11 Sectional views of computational grids.

lacking viscous modeling in the computations. As Fig. 12 demonstrates, from $2x/B = 23.7\%$ to 59.8%, the area of the flap cutout bears the stronger separation tendency due to the missing flap effect. The wing without the flap has a few different pressure distributions. Figures 13a and 13b show respectively the sectional grids and the corresponding computed Mach contours at midspan location. The recirculating area and the low Mach numbers in the main element cove are vividly visible in Fig. 13b.

Lift coefficients vs AOA (angle of attack) are plotted in Fig. 14 with comparisons to experimental data. The whole lift curve in the computation results is higher than in experimental results by 0.10. The reason is attributed to the occurrence of flow separation because the wing with flaps is more likely to cause flow separation. It is believed that the present Euler flow solver cannot appropriately calculate and analyze the flow separation accurately. Similar

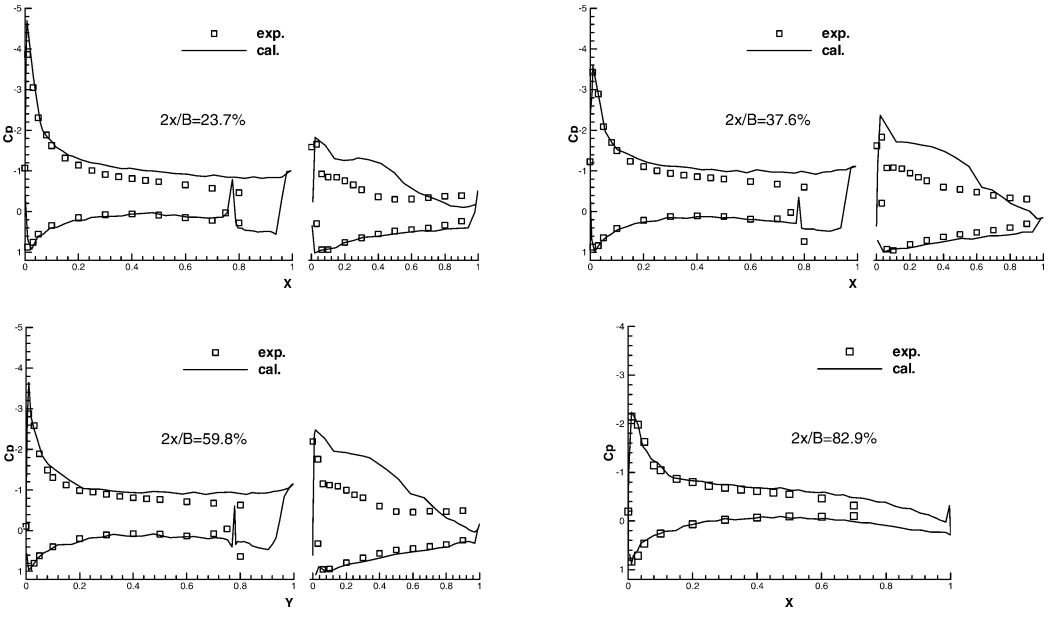

a) $M_\infty = 0.2 \cdot \alpha = 4.47°$

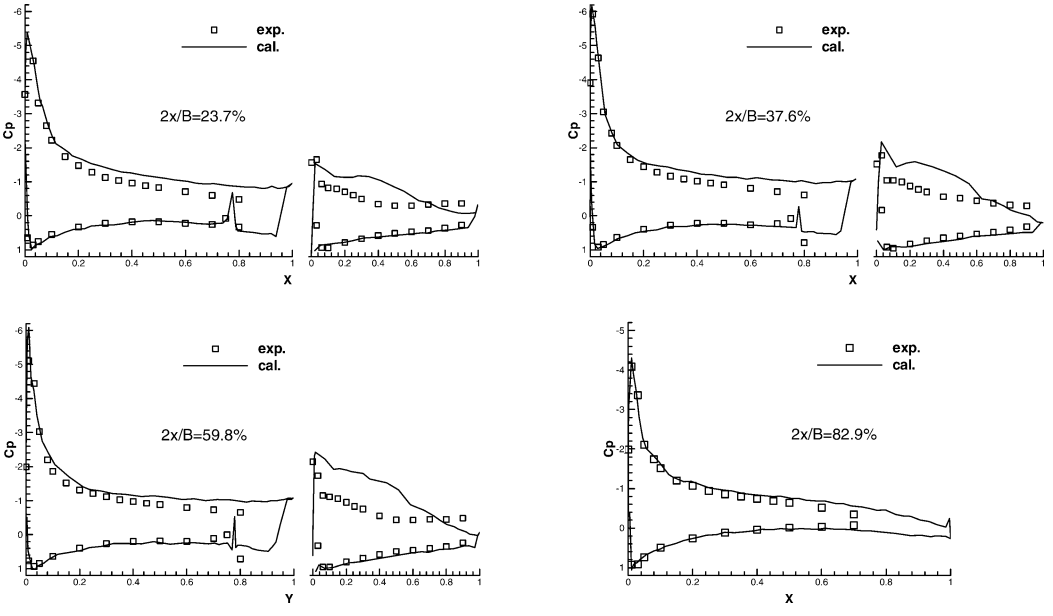

b) $M_\infty = 0.2 \cdot \alpha = 8.65°$

Fig. 12 Comparison between computed and experimental surface pressure coefficient.

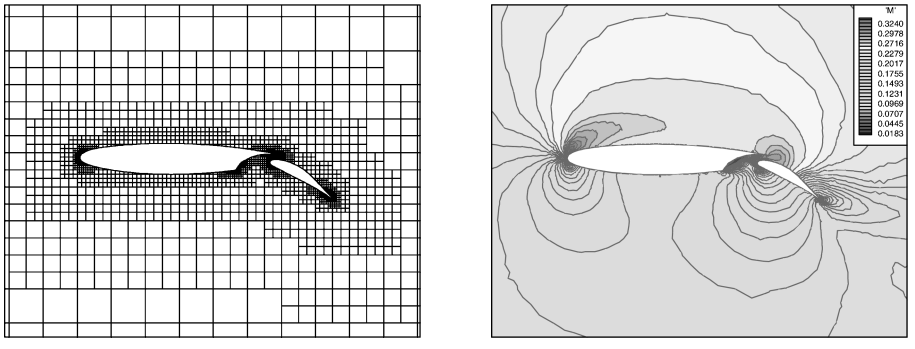

a) Computational grids **b) Computed Mach contours**

Fig. 13 Grids and Mach contours at midspan location.

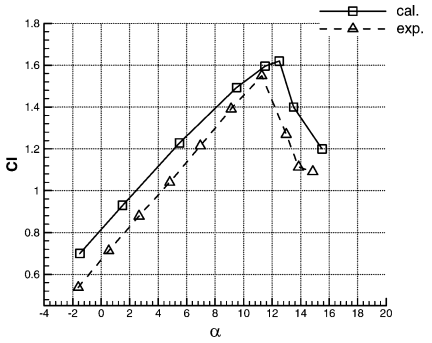

Fig. 14 Computed lift coefficients vs AOA.

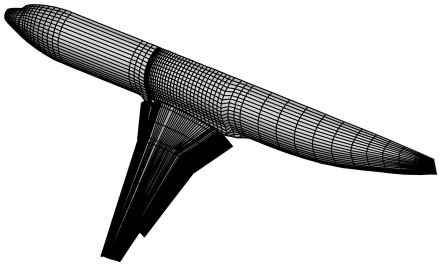

Fig. 15 Model geometry.

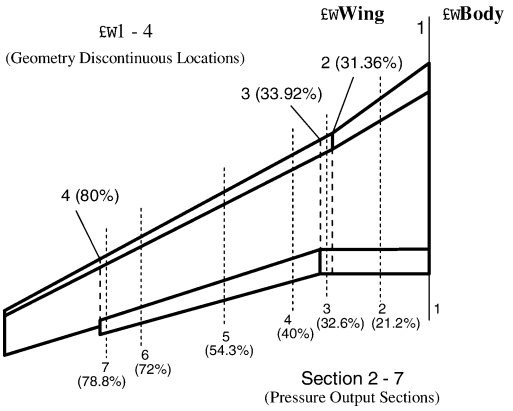

Fig. 16 Planform view for the multielement wing.

problems can be found in the results of other cases. All of these disagreements demonstrate the inadequacy of applying the present Euler flow solver to a massive separation flow. For this problem, we have more discussion in the later conclusions.

Case 3: High-Lift Transport Configuration

The model is a wing/body combination model that originated from the now-abandoned Chinese AE-100 airliner. For purpose of the high lift, the supercritical wing has been reshaped to host deployable slats and single-slotted flaps. A sketch of the model setup is shown in Fig. 15. The inboard/outboard segmentation of slat and flap is located at about 31 and 33% half span. The outboard flap ends at 80% half span, and the slat extends up to the blunt wing tip. For the present investigation, the landing configuration is considered, characterized by the slat with a deflection angle of 25 deg and the flap with a deflection angle of 40 deg. Figure 16 shows a planform view of the wing with flaps and slats and the spanwise locations where surface pressure measurements were acquired.

The model has been also experimentally studied in the low-speed wind tunnel at NUAA. In the model test, measurements were taken at freestream Mach number 0.2. In the grid generation and flow computation, the wind-tunnel wall is not considered because the experimental results are claimed to have wall interference corrected.

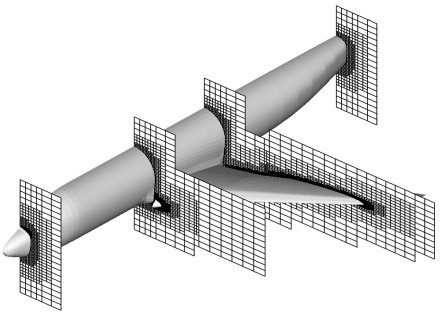

a) Axial sectional view

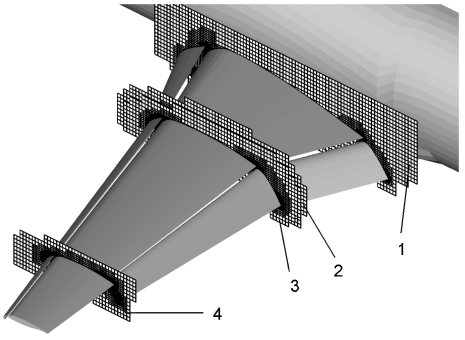

b) Cross-sectional view

Fig. 17 Sectional views of computational grids.

According to the shape of the configuration, the adaptive grid technique based on the geometry is finished three times to adjust grid density and spacing near the boundaries of the model. In the present computation, a total of 6.5×10^5 grid cells in six zones are employed to simulate the model. The six zones are generated from four discontinuous locations and one wing-tip section. Figures 17a and 17b show several spanwise profiles of the spatial grids. It is easy to see that grid density increases gradually from outer to inner layer to ensure appropriate grid resolution for regions with different characteristic geometry and flow scales. The figure provides a good global view of the grid adaptive locations, as well as the grid cells with variable aspect ratio.

Figures 18a and 18b show two cases of the treatment of geometric discontinuity in the model. Therefore, the face-to-face technique is adopted and the first and fourth multizone interfaces are laid here for exchanging flow field information between adjacent zones.

The selected flow conditions refer to conditions in the wind tunnel. Figures 19a and 19b illustrate a comparison of the computed surface pressure coefficient C_p variation with the experimental data at the six spanwise sections shown in Fig. 16. For the pressure distribution, the agreements with experimental data are good on the whole. Some disagreements exist at the upper surface of the flap. Another small discrepancy in the results occurs at the trailing edge of the main wing. Besides the accuracy of the present method, an insufficient number of pressure transducers may also be responsible.

The present code is currently run in a scalar manner, although it is inherently easy to modify to a parallel version. The three numerical calculations in the current study were performed on a Pentium4 2.0GHz class personal computer with 1GB main memory.

For Case 3 as a reference frame, it took the author about a work week to set up the geometry and test Cartesian grid generation code about this configuration. Based on this work, the automatic grid generation of the models can be finished easily. For example, the grid generation for case 1 can be done in 30 min; cases 2 and 3 take about 45, and 80 min, respectively. In the light of flow analysis, the present method has high efficiency to provide a powerful tool for Cartesian grid generation for more complex high-lift configurations. Under existing computer conditions, it takes about 3 h of CPU time to run 1500 iterations to converge for the case 1

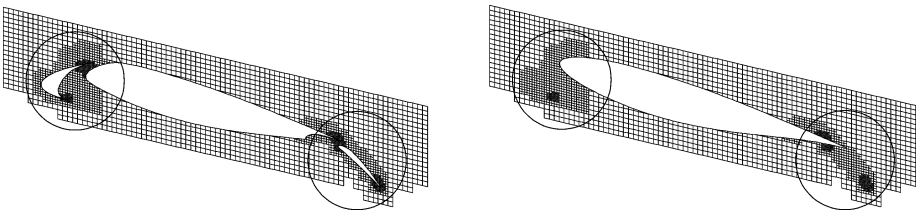

a) At the first multizone interface

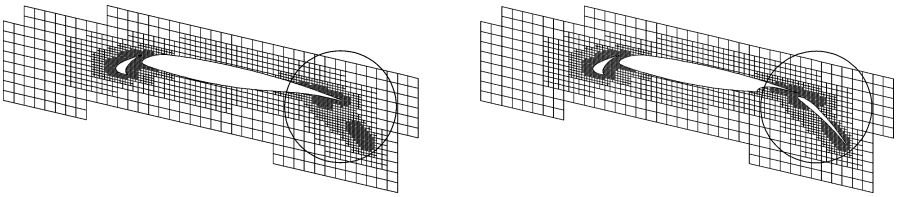

b) At the fourth multizone interface

Fig. 18 Comparison of grid sections at the first and fourth multizone interfaces.

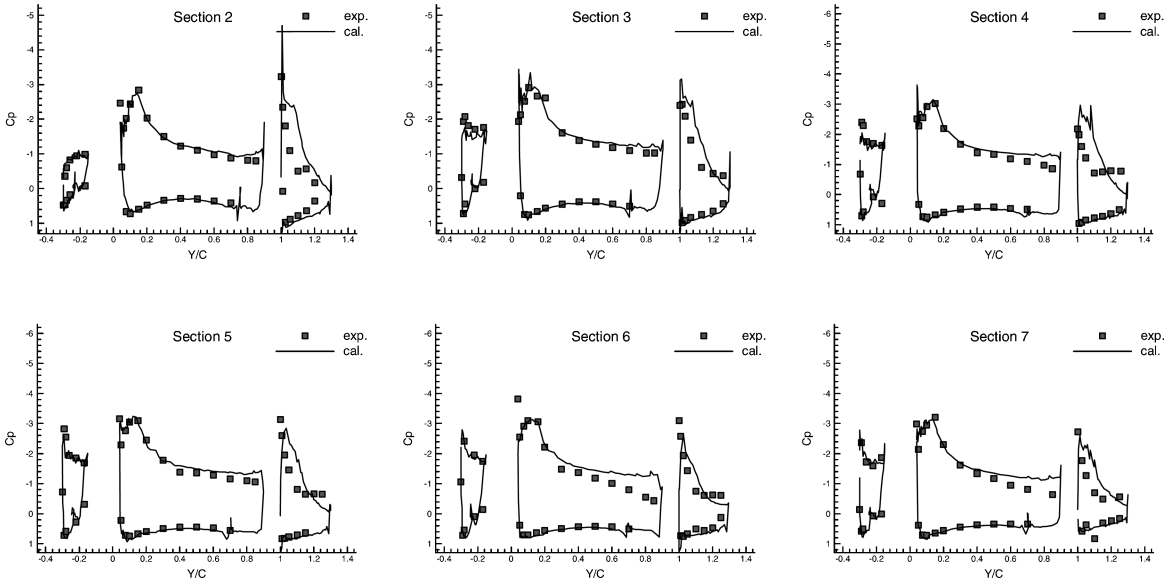

a) $M_\infty = 0.2$, $\alpha = 9.0$ deg

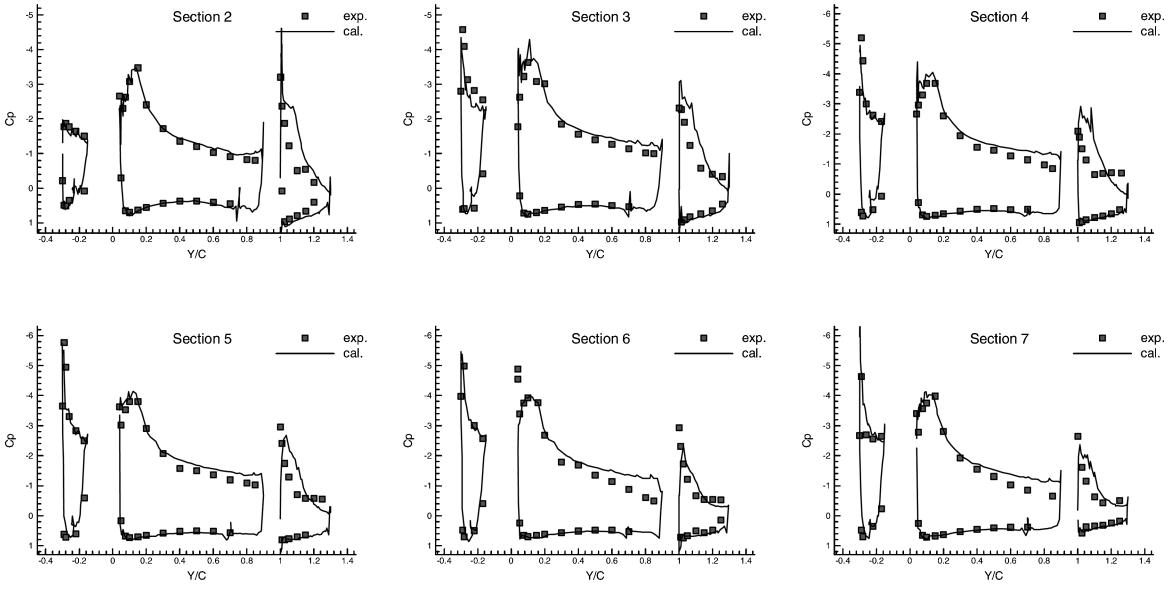

b) $M_\infty = 0.2$, $\alpha = 13.0$ deg

Fig. 19 Comparison between computed and experimental surface pressure coefficients.

model in flow simulation. However, cases 2 and case 3 take about 8 and 17 h, respectively, for approximately 3000 time steps to converge.

Conclusions

The paper describes the work of CFD improvement in the numerical simulation of high-lift configurations with respect to the adaptive Cartesian grid method and the Euler flow solver. The main emphasis is on some methods and techniques for treating geometric discontinuity in three-dimensional high-lift systems.

The feasibility of the present methods in dealing with geometric discontinuity is verified. Computations of the three-dimensional high-lift configurations are conducted using the above methods and techniques. The adaptive grid technique is applied to adjust grid density and ensure the necessary grid resolution at key flow region. The multizone technique greatly reduces the difficulties of the Cartesian grid generation. The face-to-face technique makes the numerical simulation of geometry discontinuity very simple. Investigating three high-lift configurations and comparing the results to existing experimental data validate the Euler flow solver with the dual-time stepping scheme. The codes and methods provide a good platform for examining and simulating complex flow field over the three-dimensional high-lift configurations with geometry discontinuity. This study extends previous high-lift CFD research on the adaptive Cartesian grid method, and applies to complex three-dimensional high-lift flow problems.

In the future, much work on the flow solver has to be done to improve the accuracy and reliability of the present computational results. Limited by computer resources, the present computations employ a relatively small number of grid cells. In addition to poor grid density, the viscous effect is a primary factor in flow solvers that may be responsible for the disagreement between computational results and experimental data. Therefore, the computation of Navier–Stokes equations is believed to be a good measure. This work is now under way.

References

[1]John, C. V., "An Unstructured-Mesh Euler Method for Multielement Airfoil Geometries," AIAA Paper 90-3051, Aug. 1990.

[2]Pirzadh, S., "Unstructured Viscous Grid Generation by Advancing-Layers Method," AIAA Paper 93-3453, Aug. 1993.

[3]Anderson, W. K., and Bonhaus, D. L., "Numerical Study To Assess Sulfur Hexafluoride as a Medium for Testing Multielement Airfoils," NASA Technical Paper 3496, June 1995.

[4]Lindblad, I. A. A., and de Cock, K. M. J., "CFD Prediction of Maximum Lift of a 2D High Lift Configuration," AIAA Paper 99-3180, June 1999.

[5]Rogers, S. E., "Progress in High-Lift Aerodynamics Calculations," *Journal of Aircraft*, Vol. 31, No. 6, 1994, pp. 1244–1251.

[6]Peter, E., "CFD Improvement for High Lift Flows in the European Project Eurolift," AIAA Paper 2003-3795, June 2003.

[7]Rudnik, R., Melber, S., Ronzheimer, A., and Brodersen, O., "Three-Dimensional Navier–Stokes Simulations for Transport Aircraft High-Lift Configurations," *Journal of Aircraft*, Vol. 38, No. 5, 2001, pp. 895–903.

[8]Mathias, D. L., Roth, K. R., Ross, J. C., Rogers, S. E., and Cummings, R. M., "Navier–Stokes Analysis of the Flow about a Flap Edge," AIAA Paper 95-0185, Jan. 1995.

[9]Cao, H. V., Su, T. Y., and Rogers, S. E., "Navier–Stokes Analysis of a 747 High-Lift Configuration," AIAA Paper 98-2623, June 1998.

[10]Sang, W., and Li, F., "Omni-Tree and Adaptive Cartesian Hybrid Grid Method in Steady and Unsteady Flows," AIAA Paper 2003-4078, June 2003.

[11]Kathong, M., Smith, R. E., and Tiwari, S. N., "A Conservative Approach for Flow Field Calculation on Multiple Grids," AIAA Paper 88-0224, Jan. 1988.

[12]Stolcis, L., and Johnston, L. J., "Solution of the Euler Equation on Unstructrued Grids For Two-Dimensional Compressible Flow," *Aeronautical Journal*, Vol. 94, No. 936, 1990, pp. 181–195.

[13]Gaitonde, A. L., "A Dual-Time Method for the Solution of the Unsteady Euler Equations," *Aeronautical Journal*, Vol. 98, No. 978, 1994, pp. 283–291.

[14]Arnone, A., Liou, M. S., and Povinelli, L. A., "Integration of Navier–Stokes Equations Using Dual Time Stepping and a Multigrid Method," *AIAA Journal*, Vol. 33, No. 6, 1995, pp. 985–990.

[15]Takallu, M. A., and Laflin, K. R., "Reynolds-Averaged Navier–Stokes Simulations of Two Partial-Span Flap Wing Experiments," AIAA Paper 98-0701, Jan. 1998.